PROCEEDINGS, TOUGH Symposium 2006
Lawrence Berkeley National Laboratory, Berkeley, California, May 15–17, 2006

MODELING CO_2 INJECTION WITH HALITE PRECIPITATION USING AN EXTENDED VERMA & PRUESS POROSITY-PERMEABILITY MODEL

Michele Carpita, Thomas Giorgis, Alfredo Battistelli

RISAMB Dept., INFRAMB Div., Snamprogetti SpA (ENI Group)
Via Toniolo 1, Fano (PU), 61032, Italy
e-mail: michele.carpita@snamprogetti.eni.it, thomas.giorgis@snamprogetti.eni.it,
alfredo.battistelli@snamprogetti.eni.it

ABSTRACT

The precipitation of halite around a CO_2 injection well has been studied to investigate the possible effects on well injectivity decline for a pilot test concerning the CO_2 injection in a depleted gas reservoir. The numerical simulations performed with TMGAS, a version of the TMVOC simulator with 1D and 2D radial systems, show that the injection of dry supercritical CO_2 vaporizes the formation brine promoting the NaCl concentration and the precipitation of halite. Different behaviors are observed depending on the initial liquid saturation: when the brine has a low mobility, the evaporation front advances with limited halite precipitation and only minor effects on well injectivity. On the other hand, when the brine has enough mobility, the precipitation front is recharged by the brine flowing towards the wellbore, due to the strong capillary pressure gradient driven by the evaporation. In this case the concentrated precipitation can strongly reduce the formation permeability. These effects depend on formation properties and on the porosity-permeability relationship which describes the effects of halite precipitation. In the attempt to improve the prediction of halite precipitation effects, an extension of the so-called *tube in series* model of Verma and Pruess was developed, with pore size distribution evaluated from the measured grain size distribution of the sandy formation considered for execution of the pilot CO_2 sequestration test.

INTRODUCTION

Precipitation of salts, mainly consisting of halite, is a known source of formation damage around producing wells during the exploitation of gas reservoirs when high salinity brine is present (Kleinitz et al., 2001). The precipitation is driven by the concentration of salt in the brine following water evaporation, since an higher content of water vapor is allowed in the natural gas as pressure declines. Similar problems are documented for injection wells in gas storage operations, where dry natural gas is injected in saline aquifers (Lorentz and Muller, 2003). The salt precipitation may produce a severe loss of well injectivity which eventually results in a complete blockage of injection. Modeling of water evaporation due to dry gas injection is limited in the oil industry literature (Zuluaga and Lake, 2004), whereas modeling of halite precipitation is usually not supported by numerical simulators conventionally used for hydrocarbon reservoir engineering.
These modeling capabilities, originally developed for simulators used in geothermal reservoir engineering (Verma and Pruess, 1988; Battistelli et al, 1997; Pruess et al., 1999), were recently applied to study the geological sequestration of greenhouse gases. Pruess and Garcia (2001) showed that the injection of dry CO_2 in a saline sandstone aquifer generates the persistent evaporation of water around the injection well, in addition to the displacement of formation brine down to irreducible saturation values. This causes an increase in salt concentration until it precipitates as halite, with consequent reduction in porosity and related rock permeability.

In order to study the feasibility of CO_2 sequestration in gas reservoirs we use TMGAS, a specialized version of TMVOC code (Pruess and Battistelli, 2002; Battistelli et al., 2003), belonging to the TOUGH2 family of numerical reservoir simulators. TMGAS, which is still under development, can simulate the two-phase flow of a gas mixture in equilibrium with a sodium chloride brine, including the modeling of halite precipitation/dissolution following the EWASG approach (Battistelli et al., 1997). In particular, the EWASG approach describes the permeability reduction due to the precipitation of halite using idealized models of the pore network presented by Verma and Pruess (1988). Simple relationships are derived to evaluate the permeability reduction from the residual porosity available for fluid flow.

The simulation of supercritical CO_2 injection in a depleted gas reservoir was already simulated with TMGAS (Battistelli et al., 2005) using a simple 1D radial homogeneous layer and the original *tube-in-series* model of Verma and Pruess (V&P model). The simulations showed that halite can precipitate even when injecting dry CO_2 in a depleted gas reservoir where a medium salinity brine is present. Further simulations using a more realistic 2D radial model have been performed to properly account for the gravity effects on both the initial brine saturation distribution and on the gravitational segregation of

injected high density CO_2 plume (Giorgis et al., 2006).

Here we present the results of simulations dealing with dry CO_2 injection in a radial 2D depleted gas reservoir using an extension of the original V&P permeability-porosity model. The model extension was performed in the attempt to improve the description of halite precipitation effects using a more general pore network model, to better capture the behaviour of real porous media. In fact, the permeability reduction effects depend not only on the overall porosity reduction, but also on details of the pore space geometry and the distribution of precipitate within the pore space. The model of pore network used is described here below.

THE EXTENDED V&P MODEL

The V&P pore network model describes the porous medium as a composition of channels whose axis is parallel to fluid flow. Each channel is made of two series-connected distinct pores, each of them with a different diameter, which follows a simple size distribution. The smallest pore of the series controls channel permeability, while the biggest one controls channel porosity. Channels may have a round or rectangular cross section, in order to account for cylindrical pores or for fractures. Figure 1 shows the graphical representation for a round and rectangular flow channel:

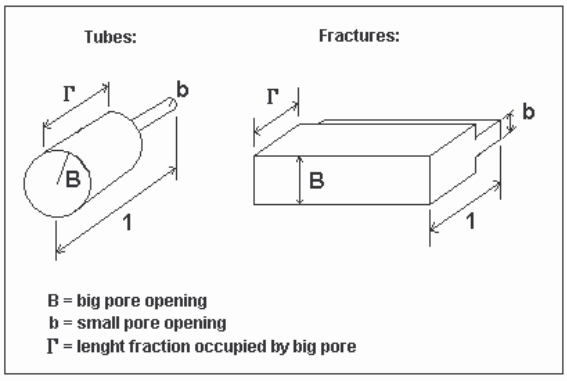

Figure 1. Pore shapes and geometrical parameters for V&P basic model (modified after Verma and Pruess, 1988).

According to the picture's scheme, *b* and *B* are the pore couples radii, while Γ is the length ratio between larger and smaller pores within a single channel. Basic pore size distributions in V&P model include linear, triangular and Gaussian functions h(b) or h(B), where b and B variability range is comprised between 0 and the maximum pore opening value in the distribution, namely *a* and *A*. The same distribution function applies to both pores of a single channel. V&P original model provides analytical solutions for pore network porosity and permeability values.

Our model extends the capabilities of the original V&P model by means of a numerical approach. This allows to consider two different pore size distributions for each component of a single channel. Moreover, channels may be built by a great number of τ identical couples, in order to consider the influence of cross-flow pore walls as well. Figure 2 shows the general shape of a single flow channel of cylindrical section. Notice that if the number of couples in a single channel becomes very large, then the channel behaviour with respect to the clogging processes tends to be similar to that of a single small pore which crosses the whole channel length, as is intuitively shown in the right picture of Figure 2.

Thanks to the numerical approach, distributions themselves may have any kind of functional form, including those coming from experimental data.

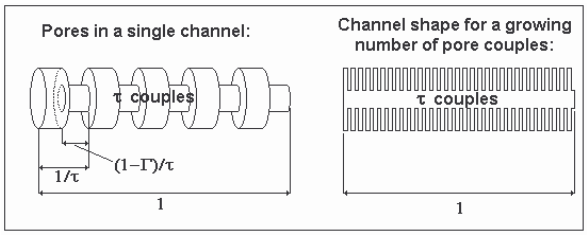

Figure 2. General shape of a single flow channel in the extended V&P model.

Estimation of Pore Size Distribution

Using the experimental measurements of the grain size distribution available for the sandy formation considered for a pilot CO_2 injection test, a simple model capable of estimating pore size distribution from grain size distribution was developed. The model is suitable for granular media and exploits the following analytical formula relative to 3 tangent spheres:

$$\frac{1}{r_4} = \left[(r_2 r_3 + r_1 r_3 + r_1 r_2) + 2\sqrt{r_1 r_2 r_3 (r_1 + r_2 + r_3)}\right] \frac{1}{r_1 r_2 r_3} \quad (1)$$

where r_4 is the radius of the sphere which might be included in the open space between three tangent spheres of r_1, r_2, r_3 radii, respectively.
Assuming r_1, r_2, r_3 radii to be the grain classes radius of a known porous media, it is possible to evaluate each *B* radius of the large pore distribution by cyclically varying the value of r_1, r_2, r_3 radii in eq. 1. The associated *h(B)* frequency value is estimated considering it to be proportional to the product of each single grain classes distribution in eq. 1. The *h(b)* small pore distribution is determined by the *h(B)* distribution by means of a suitable scaling factor.

Figure 3 shows the experimental grain classes distribution used to evaluate the pore size distribution: Figure 4 shows the results of the full pore distribution versus small and large pore openings *b* and *B*, as estimated from the model described above. This one depends also on the initial value of Γ and the ratio *a/A*. These parameters are evaluated according to further assumptions on the pore network geometry.

The numerical approach requires the discretization of the *H(B,b)* distribution. The function domain is so subdivided into a discreet number of cells. Each cell corresponds to a couple of *B* and *b* pore radii values belonging to a subdivision of the pore aperture ranges [0, *a*] and [0, *A*] in a given number of classes. We found that if the number of classes is equal or higher to 30 for each pore type, the difference between the analytical *H(B,b)* distribution and its discretized simplification becomes unimportant.

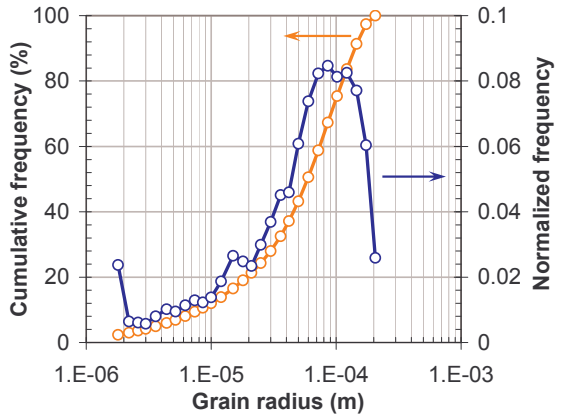

Figure 3. Mean grain size distribution of the sandy formation considered for a pilot CO_2 injection test.

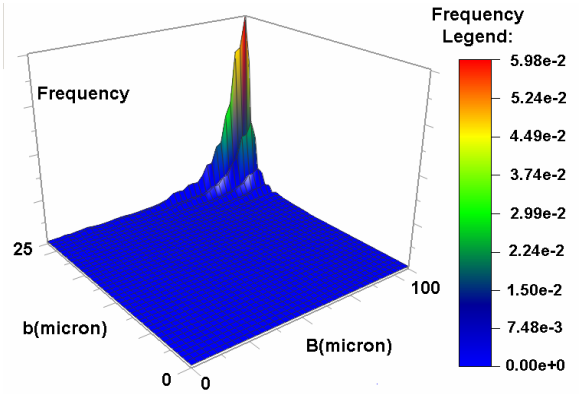

Figure 4. Pore size distribution evaluated according to the V&P extended model obtained starting from the experimental grain size distribution.

Precipitation Model

In order to account for a progressive pore filling process, a simple iterative model is used based on the assumption of an uniform precipitation layer of thickness Λ deposited along the pore walls of a single channel. This numerical approach leads to the following reduction equations of pore dimensions:

$$b_{n+1} = b_n - \Lambda \quad (2)$$

$$B_{n+1} = B_n - \Lambda \quad (3)$$

$$\Gamma_{n+1} = \Gamma_n - \Lambda \quad (4)$$

Notice that the pore filling process on cross sectional walls leads to the reduction of larger pore lengths to the advantage of smaller pores. Figure 5 shows the difference between a filling mechanism that does not take into account the cross sectional pore walls and the general filling model that instead, considers the complete surface filling of pore walls.

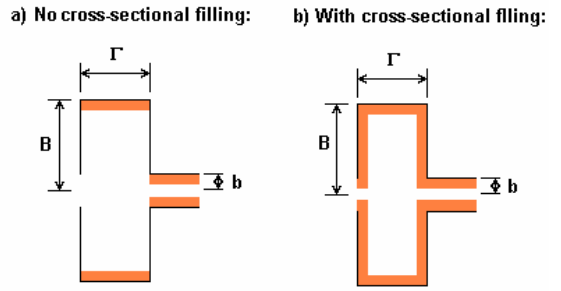

Figure 5. Clogging process neglecting and considering the scale precipitation on the cross sectional pore walls.

Permeability Versus Porosity Relationship

The above model allows to estimate both the porosity and permeability of the pore network via numerical computation. The extended V&P general expression for pore network porosity and permeability are given below:

$$\varphi(a,A) = \int_0^a db \int_b^A H(B,b)\left[\Gamma S_B + (1-\Gamma)S_b\right](N - N_\Delta)dB \quad (5)$$

$$K(a,A) = \int_0^a db \int_b^A H(B,b)\left[\frac{1-\Gamma}{k_b} + \frac{\Gamma}{k_B}\right]^{-1}(N - N_\Delta)dB \quad (6)$$

Where *N* is the number of pores per unit surface, N_Δ is the number of precipitation-clogged pores per unit surface, S_b and S_B are small and large pore cross sections respectively, and *H(B,b)* is the distribution function of pore couples of *B* and *b* radii. The variables k_b and k_B are the single pore couple permeabilities, which are given by $k_{Tb} = \frac{\pi b^4}{8}$ and $k_{Fb} = \frac{b^3}{12}$ for a round and a rectangular pore section, respectively. The discretization of the two above equations turns the integrals into sums, while *H(B,b)* is divided into a series of discrete domains as described in the previous paragraph.

In order to implement the permeability-porosity relationship numerically evaluated with the extended V&P model into the TMGAS code, the relationship proposed by Xu and Pruess (2004) was considered:

$$\frac{k}{k_0} = \left[\frac{\varphi - \varphi_C}{\varphi_0 - \varphi_C} \right]^{\eta} \qquad (7)$$

where φ_0 and k_0 are the initial porosity and permeability values before the start of the precipitation process, while φ_c is the so-called "residual porosity" which is the porosity value when pore network permeability drops to zero. η is a suitable exponent that, in the present approach, is treated as a matching parameter. The extended V&P model allows to give an estimate for φ_c by calculating the residual pore space left when the smaller pores are completely clogged by the precipitation process. By plotting the permeability versus porosity data corresponding to a progressive increase of pore filling, it is possible to obtain a satisfactory fit of numerical results with eq. 7, thus determining the suitable value of the η exponent that can be used as an input parameter inside TMGAS along with φ_0, k_0 and φ_c .

MODELING OF HALITE PRECIPITATION DRIVEN BY DRY CO_2 INJECTION

The effects of halite precipitation described with the extended V&P pore network model are presented for two simulation cases: case A and B with initial liquid saturation of 0.15 and an average of 0.60, respectively. The brine is immobile in Case A, whereas it has sufficient mobility to flow in Case B.

Numerical Model

An idealized model is used, consisting in a gas reservoir emplaced in a sand formation simulated as a horizontal disc with thickness of 10 m and an external radius of 10 km. The disc is discretized with a 2D radial grid, with the well of 0.2 m diameter located on the axis of symmetry. A fine radial grid is used close to the well sandface starting with an element of 0.01 m width, then increasing the elements width following a logarithmic progression. The vertical discretization is made up of 10 grid layers of constant thickness of 1 m. The upper and lower boundaries of the domain are closed, whereas constant conditions are maintained at the lateral boundary. The petrophysical parameters are representative of a sand layer present in an exploited gas reservoir presently considered in Italy for a pilot CO_2 injection test. The porosity is 0.32, the horizontal permeability is 400×10^{-15} m^2, while the vertical one is about 40×10^{-15} m^2. Initial reservoir conditions are 45°C and 60 bar abs. The natural gas has the following dry molar composition: CH_4 92.78%, ethane 4.58%, propane 2.60%, CO_2 0.04%, where the propane is actually a pseudo-component for propane and heavier alkanes. Brine molality is 1.76 mol/kg. The experimental capillary pressure data shown in Figure 6 were fitted using Van Genuchten's model (VG), whereas gas and liquid relative permeabilities data, shown in Figure 7, were fitted with the Corey and VG models, respectively. The aqueous phase irreducible saturation is 0.20, but the liquid relative permeability remains very low up to saturations of 0.60.

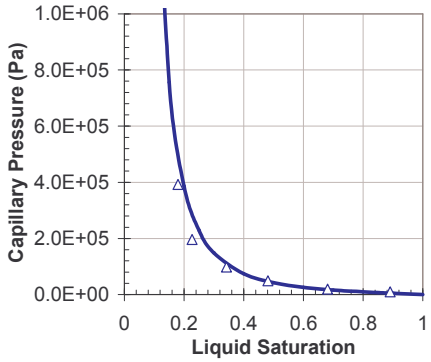

Figure 6. Capillary pressure curve: symbols = experimental data; line = VG's model.

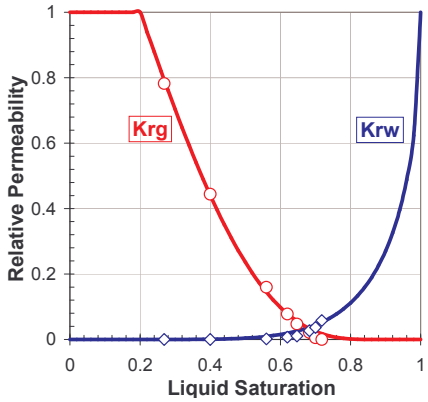

Figure 7. Relative permeability curves: symbols = experimental data; lines = fitting curves with Corey's (gas phase) and VG's (aqueous phase) models.

The amount of precipitated salt is described in terms of solid saturation, that is the fraction of pore volume occupied by halite. To describe the permeability reduction as a function of porosity reduction the extended V&P model is used. For the considered pore size distribution, the absolute permeability of porous medium becomes zero when the porosity is reduced to 30% of its original value, that is when the solid saturation reaches 0.70. The permeability-porosity relationship calculated with the extended V&P model is plotted in Figure 8. A regression made using the Xu and Pruess relationship (eq. 7) allows to determine the exponent value η , which in this case is equal to 4.1 . The regression function is shown as a

solid line in Figure 8.

The simulations are all performed assuming isothermal conditions, neglecting the thermal effects associated to water vaporization, compression and decompression of CO_2 and the heat of solution of gases in the brine. The vapor pressure lowering (VPL) due to capillary effects is neglected; the VPL reduces the brine vapor pressure (Battistelli et al., 1997) and, as a consequence, reduces the water evaporation at strong capillary pressure values. In the present version of the TMGAS code, the gas phase properties are calculated using an equation of state developed by LBNL called GASEOS. The Henry's law including the salting-out effect is still used to evaluate the solubility of gases in the brine, overestimating their solubility in the aqueous phase at high pressure. Moreover, the water content in the CO_2-rich phase is still evaluated as an evaporation process which underestimates the solubility of water in the gas phase. The molecular diffusion is simulated using the Fickian approach available within TOUGH2. The above assumptions affect the impact of different processes, but do not substantially alter the overall system behavior. A constant rate of 1 kg/s CO_2, which is in the range considered for the pilot injection test, is simulated for a period of 2 years by injecting in the upper element of the well.

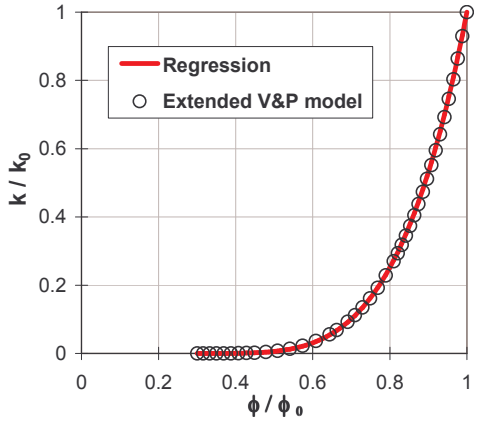

Figure 8. Porosity-permeability relationship: symbols = extended V&P model; line = regression curve using the Xu and Pruess equation.

1D Simulations with the Original V&P Model

For an easier comprehension of the near wellbore processes driven by the injection of dry CO_2 in a natural gas reservoir it is interesting to review the main results obtained by modeling the same formation with a 1D radial grid (Battistelli et al., 2005). Even though the original V&P model was used for the 1D simulations, the relative permeability-porosity relationship is actually very close to that shown in Figure 8: the considerations made for the 1D grid can then be extended to the 2D grid. The model geometry, as well as the petrophysical properties, the thermodynamic conditions and the injection rate, are the same used for the 2D simulations. When the dry CO_2 contacts the reservoir brine, being the liquid phase immobile (Sw=0.15), the water vaporizes into the CO_2-rich phase until there is a complete disappearance of the aqueous phase. The precipitation of halite is limited by the amount of NaCl initially stored per unit pore volume. In this case the evaporation/precipitation front travels inside the formation with limited effects on the injection performances.

When the brine is mobile (Sw=0.50) the behaviour of evaporation/ precipitation front is quite different. The continuous injection produces the concentration of NaCl, which eventually reaches the saturation with the precipitation of solid halite. The decrease of brine saturation produces a capillary pressure gradient towards the well sandface which may overcome the injection pressure gradient and thus can drive a counterflow of brine towards the evaporation/ precipitation front. Depending on the rates of water evaporation and brine counter-flow, the evaporation/ precipitation can advance so slowly that a concentrated salt precipitation occurs at and near the wellbore sandface, with clogging of the porous medium. Figure 9 shows the time evolution at the sandface element of some reservoir parameters during CO_2 injection when the aqueous phase is mobile. The evaporation at the sandface reduces the aqueous phase saturation increasingly and generates a capillary pressure gradient close to the evaporation front which overcomes the injection pressure gradient. Around the well as shown in Figure 10, the brine flows back to the evaporation front supplying water for the evaporation process. Halite precipitation persists at the evaporation front due to the supply of salt carried by the brine flow: in these conditions the solid saturation increases and reduces the rock permeability to values which make it impossible to continue the injection operations.

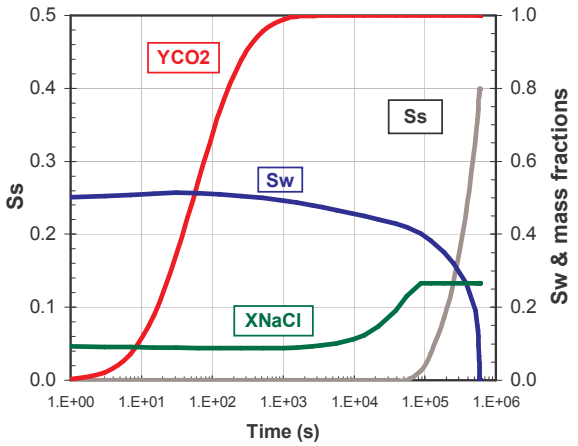

Fig. 9. Mobile brine: time evolution of aqueous and solid saturations, CO_2 mass fraction in the gas phase and NaCl mass fraction at the sandface element.

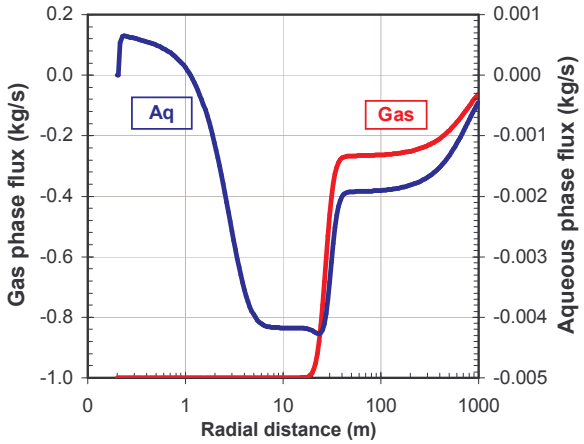

Fig. 10. Mobile brine: radial distribution of aqueous and gas phase fluxes after 8 days of injection (positive fluxes are directed toward the well).

For the investigated formation properties, the injection of dry CO_2 has been simulated by determining, for a given injection rate value, the initial saturation of the aqueous phase at which the complete clogging of the formation is observed (threshold saturation value). The results plotted on Figure 11 show that the threshold value increases with the injection rate: no clogging occurs even for the injection in a brine saturated formation when the rate is above 1.5 kg/s. The rate dependent threshold value of initial liquid saturation is useful to interpret the injection behavior of the radial system when it is discretized using a 2D grid.

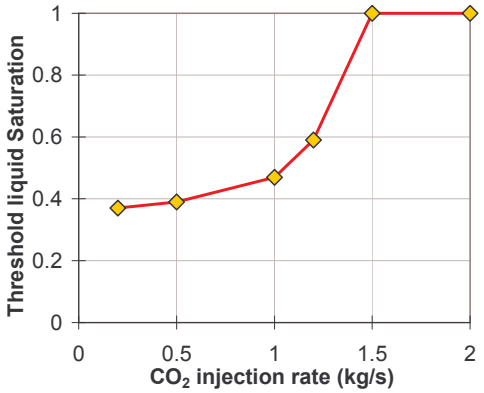

Figure 11. Dependence of the threshold value of initial liquid saturation from CO_2 injection rate (10 m pay thickness).

2D Simulation Results with the Extended V&P Model

The results obtained by simulating the same radial system with the 2D grid are now presented for Cases A and B. They can be representative of two possible locations of the CO_2 injection well, where Case B represents the injection in a zone of the depleted gas reservoir invaded by the lateral aquifer.

Case A: immobile brine

Injected CO_2 equally flows from the wellbore in each layer in which the system is discretized. As the water phase is immobile, the evaporation and precipitation fronts advance with similar velocity in each grid layer in the radial direction. The halite precipitation is uniformly distributed as shown in Figure 12.

The displacement front of the CO_2 rich gas phase (density of 147 kg/m^3) advances preferentially on the bottom of the formation by density driven flow, displacing the lighter reservoir gas (density of 45 kg/m^3). At longer injection times, the density driven flow predominates at the injection plume front, as shown in Figure 13, as the injection pressure gradient becomes lower and lower in a radial system.

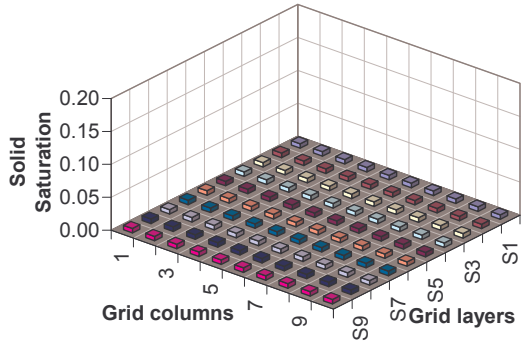

Figure 12. Spatial distribution of solid saturation after 6 months of CO_2 injection to a radial distance of 0.32 m (grid columns = Nr. of discretization column from the sandface; grid layers = Nr. of discretization layer from the top).

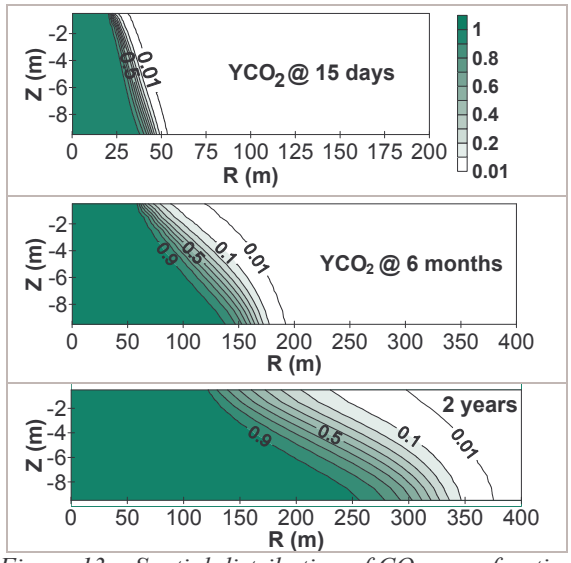

Figure 13. Spatial distribution of CO_2 mass fraction in the gas phase at different injection times (Case A).

The precipitation front, much slower than the displacement one, after 2 years of injection reaches a radius of 5 m, traveling inside the formation with

limited effects on the injection performances, as the halite solid saturation is constrained by the amount of NaCl initially present in the immobile brine per unit pore volume. In this case the porosity reduction is small and there is no significant change in rock permeability.

Case B: mobile brine

The initial conditions before the injection were obtained by running the model to a steady state governed by a gravity-capillary static equilibrium, starting with an average value of liquid saturation of 0.60. Final aqueous phase saturations are 0.45 and 0.85 at the top and bottom of formation, respectively. These conditions can be roughly representative of a zone of a depleted gas reservoir affected by the ingression of a lateral aquifer. The injected CO_2 plume mainly advances in the upper grid layers, where a higher gas phase mobility is present (Figure 14).

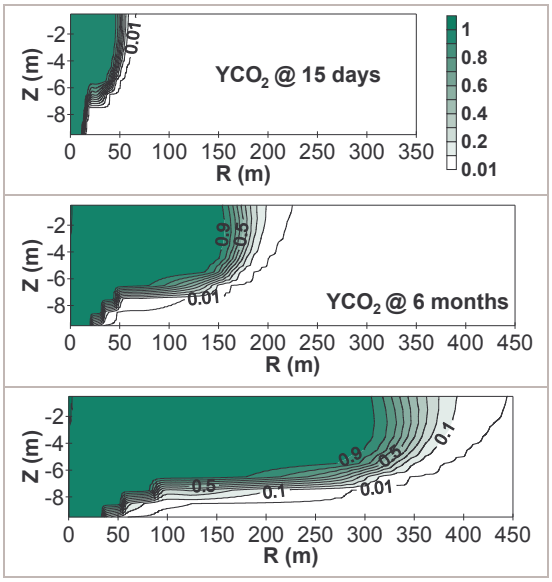

Figure 14. Spatial distribution of CO_2 mass fraction in the gas phase at different injection times (Case B).

The injected dry CO_2 produces the persistent evaporation of water around the injection well. The decrease of brine saturation produces a capillary pressure gradient which overcomes the injection pressure gradient and thus can drive a counter-flow of brine towards the evaporation/precipitation front, with an increase in salt concentration until it precipitates as halite. In all 6 deeper layers, where the aqueous phase saturation is high, the brine flow towards the well balances the water evaporation into the injected dry CO_2. The brine flow supplies both water for the evaporation and NaCl for the precipitation processes. The concentrated precipitation at the well sandface allows the halite to reach the critical solid saturation of 0.70, as shown in Figure 15 after 6 months of injection.

The injection in the lower 6 grid layers is then stopped completely. Consequently, the CO_2 injection fluxes increases in the upper 4 grid layers, as shown in Figure 16, because of the redistribution of the CO_2 injected at constant rate. In these grid layers the CO_2 advances by displacing the natural gas, as shown by the shape of the CO_2 plume in Figure 14. Thus, in the upper formation section, the evaporation and precipitation fronts can travel inside the formation with a limited reduction in porosity and rock permeability, as the evaporation process is not adequately balanced by the brine flow towards the well.

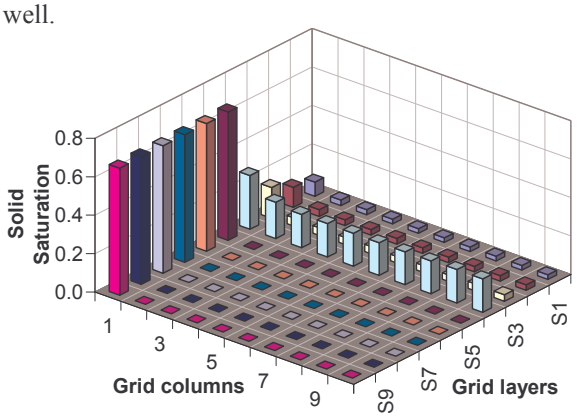

Figure 15. Spatial distribution of solid saturation after 6 months of injection to a radial distance of 0.32 m.

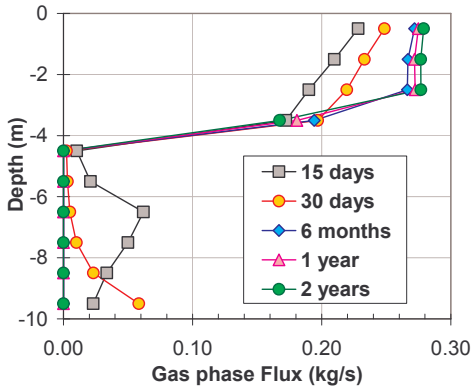

Figure 16. Vertical distribution of CO_2 well injection fluxes at different injection times.

The behavior shown by the 2D radial system is quite different from that obtained when the formation is discretized with a 1D grid. A complete formation clogging is not observed, although the initial liquid saturation is actually higher than the threshold value shown in Figure 11 for all the grid layers. The reason is the redistribution of CO_2 injection fluxes in the upper 4 grid layers due to faster clogging of the lower 6 grid layers. As shown in Figure 16, after 1 month the injection fluxes in the upper 4 grid layers are greater than 0.2 kg, which corresponds to an injection rate of 2 kg/s for 10 m pay. The threshold value of

liquid saturation is then higher, as shown in Figure 11. The higher flux in the upper 4 grid layers increases the injection pressure gradient which reduces the driving force controlling the brine flow towards the well.

The results suggest that a high CO_2 injection rate should allow to continue the injection process with limited effects on injectivity, even though important halite precipitation phenomena are present. The injection rate values required to avoid complete clogging of the sandface are of course dependent on the formation's characteristics, initial reservoir thermodynamic conditions, initial brine saturation and salinity.

CONCLUSIONS

Modeling of halite precipitation during the sequestration of supercritical dry CO_2 in a depleted gas reservoir suggests that solid NaCl (halite) precipitates even when reservoir brine is of medium salinity, as often encountered in Italian gas fields. The halite precipitation can substantially alter the formation permeability with possible effects on well injectivity decline only when the brine has enough mobility to flow under the combined effects of injection pressure and capillary pressure gradients. It is shown that the injection rate is significant in controlling the salt precipitation process and in avoiding or determining the complete clogging of formation.

Assuming sufficient initial aqueous phase mobility, the simulations show that the redistribution of CO_2 fluxes along the vertical allows to continue the CO_2 injection which is concentrated in the first layers, while in the deeper ones the evaporation-precipitation front still lies on the sandface, with an increase in salt concentration until it precipitates as halite. The porosity-permeability reduction curve actually controls the extent of formation damage induced by halite precipitation. Experimental data on pore size distribution as well as on the actual permeability-porosity relationship are necessary to validate the ability of the model to actually reproduce the formation clogging behaviour due to halite precipitation.

ACKNOWLEDGMENTS

This work was performed within the R&D project "GreenHouse Gases" financed by ENI SpA. Stogit SpA and ENI E&P Division of are acknowledged for making available the reservoir properties data. The TMGAS reservoir simulator has been developed in the frame of the R&D project "Sulphur and H_2S management in E&P operation" financed by ENI SpA. Thanks are due to George Moridis (LBNL) who made available the GASEOS suite of thermodynamical routines for the computation of real gas mixture properties.

REFERENCES

Battistelli, A, T. Giorgis, D. Marzorati. Modeling halite precipitation around CO_2 injection wells in depleted gas reservoirs. EAGE 67th Conference & Exhibition, Madrid, Spain, 13 - 16 June, 2005.

Battistelli, A., C.M. Oldenburg., G. Moridis, K. Pruess. Modeling Gas Reservoir Processes with TMVOC V.2.0, Proceedings TOUGH2 Symposium, Berkeley, Calif., May 12-14, 2003.

Battistelli, A., C. Calore, and K. Pruess. The simulator TOUGH2/EWASG for modelling geothermal reservoirs with brines and a non-condensible gas. *Geothermics, 26*,4:437 – 464, 1997.

Giorgis, T., M. Carpita, A. Battistelli, and D. Marzorati. Modeling brine evaporation and halite precipitation driven by CO_2 injection in depleted gas reservoirs, GHGT-8, 19-22 June, 2006.

Kleinitz, W., M. Köheler, and G. Dietzsch. The precipitation of salt in gas producing wells. Paper SPE 68953 presented at the SPE European Formation Damage Conference held in The Hague, The Netherlands, 21–22 May, 2001.

Lorentz, S., and W. Muller. Modelling of halite formation in natural gas storage aquifers. Proceedings TOUGH2 Symposium, Berkeley, Calif., May 12-14, 2003.

Pruess, K. and A. Battistelli. *TMVOC, a numerical simulator for three-phase non-isothermal flows of multicomponent hydrocarbon mixtures in saturated-unsaturated heterogeneous media*. Report LBNL-49375, Lawrence Berkeley National Laboratory, Berkeley, CA, 2002.

Pruess, K. and J. García. Multiphase flow dynamics during CO_2 disposal into saline aquifers. *Environmental Geology*, 42, 282-295, 2001.

Pruess, K., C.M. Oldenburg, and G. Moridis, TOUGH2 User's Guide, Version 2.0, Report LBNL-43134, Lawrence Berkeley National Laboratory, Berkeley, CA, 1999.

Verma, A. and K. Pruess. Thermohydrologic conditions and silica redistribution near high-level nuclear wastes emplaced in saturated geological formations. *J. Geophysical Res., 93*,B2:1159-1173, 1988.

Xu, T.-F. and K. Pruess. *Numerical Simulation of Injectivity Effects of Mineral Scaling and Clay Swelling in a Fractured Geothermal Reservoir*. Lawrence Berkeley National Lab., Report LBNL-56175, 2004.

Zuluaga, E, and LW. Lake. Modeling of experiments on water vaporization for gas injection. Paper SPE 91393 presented at the 2004 SPE Eastern Regional Meeting, Charleston, WV, 15-17 Sept. 2004.